Available online at www.sciencedirect.com
SCIENCE DIRECT®
Icarus 165 (2003) 355–370
ICARUS
www.elsevier.com/locate/icarus

Interacting ellipsoids: a minimal model for the dynamics of rubble-pile bodies

F. Roig,[a,*] R. Duffard,[a] P. Penteado,[a] D. Lazzaro,[a] and T. Kodama [b]

[a] *Observatório Nacional–MCT, Rua Gal. José Cristino 77, Rio de Janeiro, 20921-400 RJ, Brazil*
[b] *Instituto de Física–UFRJ, Cx. Postal 68528, Rio de Janeiro, 21945-970 RJ, Brazil*

Received 13 March 2003; revised 7 July 2003

Abstract

A simple mechanical model is formulated to study the dynamics of rubble-pile asteroids, formed by the gravitational re-accumulation of fragments after the collisional breakup of a parent body. In this model, a rubble-pile consists of N interacting fragments represented by rigid ellipsoids, and the equations of motion explicitly incorporate the minimal degrees of freedom necessary to describe the attitude and rotational state of each fragment. In spite of its simplicity, our numerical examples indicate that the overall behavior of our model is in line with several known properties of collisional events, like the energy and angular momentum partition during high velocity impacts. Therefore, it may be considered as a well defined minimal model.

Keywords: Collisional physics; Impact processes; Rotational dynamics; Asteroids

1. Introduction

Rubble-pile asteroids are believe to be the outcomes of the re-accumulation of fragments after the catastrophic disruption of a large asteroid. They would be basically constituted by a cluster of several monolithic bodies, which are kept together by their mutual gravitational attraction, without any additional cohesive forces between them. Among several evidences, the actual existence of a large number of these cohesion-less bodies in the asteroid belt is suggested by:

(i) the rather low mass densities ($\sim$ 1–2 g cm^{-3}) measured on some large asteroids (e.g., Merline et al., 1999; Veverka et al., 1997; Viateau, 2000; Yeomans et al., 1997, 1999);
(ii) the notable absence of kilometer-sized and larger bodies with rotational periods shorter than $\sim$ 2 h (e.g., Harris and Burns, 1979; Pravec and Harris, 2000; Weidenschilling, 1981);
(iii) the unusual observed shapes of some asteroids (e.g., Bottke et al., 1999; Kwiatkowski, 1995; Miller et al., 2002; Thomas et al., 2002);
(iv) the presence of giant craters and grooves on the surfaces of some asteroids recently revealed by the NEAR Shoemaker probe (e.g., Veverka et al., 1997); and
(v) the existence of small asteroidal satellites and binary asteroids (e.g., Chapman et al., 1995; Merline et al., 1999).

Many collisional processes in the Solar System, like the formation of asteroid families, the tidal disruption of comets and NEAs, and the formation of asteroid satellites, may involve parent bodies with a rubble pile structure. Thus, the precise understandings of the collisional dynamics of rubble-piles would give important insight about these processes. One of the crucial questions about the formation of asteroid families is how the incident collisional energy is transferred into the rotational energies of the ejected fragments. The purpose of this paper is to introduce a minimal model to study such problems. This model aims to describe the macroscopic behavior of different quantities—like energy, angular momentum, escape velocities and spins—during the course of the dynamical processes involving rubble-pile asteroids,

* Corresponding author.
E-mail address: froig@on.br (F. Roig).

0019-1035/$ – see front matter
doi:10.1016/S0019-1035(03)00216-1

like gravitational re-accumulation, collisional fragmentation and/or tidal disruption.

Collisional phenomena have played an important role in Solar System dynamics. There are plenty of observational evidences that collisional impacts have been decisive to shape the size, spin and orbital distributions in the asteroid belt (e.g., Durda et al., 1998), as well as to sculpt the surfaces of the inner planets and the jovian satellites. In the light of such evidence, a big effort has been done to develop physical models aiming to simulate this kind of phenomena. These goes from the statistical models describing the collisional evolution of large populations of bodies (e.g., Wetherill, 1967; Dohnanyi, 1969; Farinella and Davis, 1992), passing through analytical (Petit and Farinella, 1993) and semi-empirical (Paolicchi et al., 1989) models, to the precise numerical simulation of binary collisions (e.g., Asphaug and Scheeres, 1999; Benz and Asphaug, 1994; Benz et al., 1994; Michel et al., 2001, 2002). A similar effort has also been applied in performing scaled-down laboratory experiments, aiming to analyze the outcomes of high velocity projectiles impacting small targets of different materials (e.g., Fujiwara and Tsukamoto, 1980, 1981; Giblin et al., 1994, 1998; Love et al., 1993; Nakamura and Fujiwara, 1991; Ryan and Melosh, 1998).

The physical and dynamical characteristics of the fragments after the catastrophic breakup of a body depends mainly on the regime in which the collision occurred. For small targets, catastrophic collisions occur in a regime dominated by the tensile strength of the material, and the probability of pulverizing the target is smaller for smaller bodies (e.g., Holsapple, 1994; Housen and Holsapple, 1990, 1999; Ryan, 1992). For large bodies, the collision happens in a gravity dominated regime, and in this case, the larger the target the higher impact energy that is needed to totally disperse the fragments (e.g., Benz and Asphaug, 1999; Davis et al., 1995; Love and Ahrens, 1996; Melosh and Ryan, 1997). The transition between these two regimes seems occur around target sizes between 100 m and 1 km (e.g., Benz and Asphaug, 1999; Durda et al., 1998).

Even if Earth-based laboratory experiments allow one to analyze the possible final states of the fragments after a collision in the tensile strength regime, it is not clear whether such results can be extrapolated to large scale asteroidal collisions or not (e.g., Ryan, 1992). Therefore, in the case of collisions among kilometer-sized bodies, the only way to assess the dynamics involved is through the use of physical models.

Collisional impacts among asteroids can be grouped in three categories:

(i) cratering events, related to low energy impacts that do not breakup the target;
(ii) shattering events, that create fractures in the inner structure of the impacted body, and may eventually break it into several fragments; and
(iii) dispersing events, related to high-energy impacts that break up the target generating fragments with ejection velocities larger than the escape velocity from the impacted body.

Simulations of these kind of events have been possible in recent years thanks to the introduction of hydrodynamic models, which are mainly based on the Smoothed Particles Hydrodynamics (SPH) method (Lucy, 1977; Gingold and Monaghan, 1977). These hydrocodes assume that the colliding bodies are constituted of many thousands of small particles, and simulate the evolution of these particles according to a given equation of state that involves the tensile strength and the properties of the material (e.g., Benz and Asphaug, 1994, 1999; Love and Ahrens, 1996). SPH models have had a great success and might be considered the state of the art in simulations of collisional impacts. Another important achievement has been the introduction of very efficient gravitational N-body codes to simulate collisional processes during the accretion of planetesimals, as well as the tidal disruption of rubble-pile asteroids (Bottke et al., 1999; Leinhardt and Richardson, 2002; Leinhardt et al., 2000; Richardson et al., 2000).

In a recent work, Michel et al. (2001) combine the SPH technique with an N-body gravitational model to study the outcomes of a breakup event in the gravity dominated regime. In this model, the hydrocode is used first to impact a monolithic target and to propagate the fractures, disregarding gravitation. The outcome of this simulation is then fed into the N-body code (Richardson et al., 2000), which simulates the subsequent evolution of the system. With this model, the authors can analyze the different properties of the resulting fragments, like size distribution, ejection velocity field, as well as the processes occurring after the breakup, like gravitational re-accumulation of fragments and formation of satellites.

One of the relevant observables that carries information about the collisional processes during the formation of asteroidal families is the rotational properties of the fragments. Due to the nature of the hydrodynamic equations, the SPH models do not consider *explicitly* the rotational degrees of freedom of the fragments. In fact, the fragment's rotation appears as a consequence of the collective translational motion of re-accumulated SPH particles (e.g., Asphaug and Scheeres, 1999). Since this rotation involves an extremely complex motion of hydrodynamical origin, the SPH models are not transparent to show how the impact energy is transferred to the fragments' spins. The same kind of limitation is present in the direct N-body simulations of rubble-pile dynamics (see Richardson et al., 2003), where the rotational state of gravitational aggregates is determined by the collective translational motion of their components. Thus, in order to analyze this problem, it may be more convenient to introduce explicitly in the model the degrees of freedom related to the attitude and spin of the individual fragments from the very beginning.

Motivated by this idea, we introduce a new model based on a purely mechanical approach, without considering the thermodynamical properties of the fragments' material. We assume that the gravitational re-accumulation has already taken place, so that we start with a single rubble-pile composed of some tens or hundreds of monolithic fragments, with a given size distribution. For the sake of simplicity, we consider these fragments as rigid triaxial ellipsoids, interacting with each other via their gravitational attraction and a short-range repulsive mutual potential. Then, we obtain the Lagrangian of the system, expressed in terms of the minimal degrees of freedom that are necessary to describe the translational and rotational dynamics of each fragment. We expect that these minimal degrees of freedom were enough to reproduce the basic macroscopic dynamics during the break-up of a rubble-pile under the effect of collisions or tidal forces. It should be stressed that, differently from SPH or N-body simulations, *the present model does not intend to provide detailed simulations of a given collisional event*, neither in the gravity nor in the strength regimes. *Rather, it intends to provide a general understanding of the macroscopic processes involved in rubble-pile fragmentation*—like energy partition, angular momentum transfer, ejection velocities, and especially attitude and spin distributions of the fragments—, *in terms of the smallest possible number of degrees of freedom*.

This paper is organized as follows: In Section 2 we describe our model in detail. We introduce the interaction potential among the fragments in Section 2.1. The strategy to propagate the attitude of the fragments is presented in Section 2.2. Dissipative effects are treated in Section 2.4. Section 3 presents some numerical experiments with the model. The results are analyzed and discussed in Section 4. Finally, Section 5 is devoted to the conclusions.

2. The model

Our model is constituted by a set of N interacting rigid bodies, each of them represented by a triaxial ellipsoid of mass m_i and principal semi-axes $A_i \geqslant B_i \geqslant C_i$. The dynamical state of each ellipsoid is determined by its center of mass position $\mathbf{r}_i = (x_i, y_i, z_i)$ and velocity $\dot{\mathbf{r}}_i = (\dot{x}_i, \dot{y}_i, \dot{z}_i)$, and by the attitude of the ellipsoid $\boldsymbol{\varphi}_i = (\phi_i, \theta_i, \psi_i)$, where ϕ, θ, ψ are the Euler angles,[1] and the spin components around the principal axes of the ellipsoid:

$$\boldsymbol{\omega}_i = \begin{pmatrix} \sin\theta_i \sin\psi_i & \cos\psi_i & 0 \\ \sin\theta_i \cos\psi_i & -\sin\psi_i & 0 \\ \cos\theta_i & 0 & 1 \end{pmatrix} \dot{\boldsymbol{\varphi}}_i. \tag{1}$$

Thus, the whole system has $6N$ degrees of freedom.

The mass distribution of each ellipsoid is modeled by a Gaussian

$$\rho_i(\mathbf{r}) = \rho_{0i} \exp\left(-\kappa (\mathbf{r} - \mathbf{r}_i)^{\mathrm{T}} \mathbf{R}_i^{\mathrm{T}} \mathbf{E}_i \mathbf{R}_i (\mathbf{r} - \mathbf{r}_i)\right), \tag{2}$$

where $\mathbf{r}$ is referred to a fixed coordinate system, $\mathbf{R}_i = \mathbf{R}^z(\psi_i)\mathbf{R}^x(\theta_i)\mathbf{R}^z(\phi_i)$ is a standard rotation matrix, and the superscript $^{\mathrm{T}}$ refers to the transpose.[2] The matrix $\mathbf{E}_i$ is a purely diagonal matrix with elements $1/A_i^2$, $1/B_i^2$, and $1/C_i^2$ that characterizes the ellipsoid. The value of ρ_{0i} is chosen such that

$$m_i = \int_{-\infty}^{\infty} \mathrm{d}^3\mathbf{r}\, \rho_i(\mathbf{r}) = \sqrt{\frac{\pi^3}{\kappa^3}} \rho_{0i} A_i B_i C_i. \tag{3}$$

The constant κ, which determines the width of the distribution, will be fixed later. The use of a Gaussian mass distribution does not have any physical relation with the actual mass density of an asteroid, which is presumably constant up to its edges. As we will see later, the mass distribution is used to define the mutual short-range repulsive interaction potential between two ellipsoids. Thus, the actual form of the distribution is not important provided that this interaction potential is well defined. The simplest choice is a Gaussian function since it is very easy to manipulate. Moreover, according to this mass distribution, the principal moments of inertia around the principal axes of the ellipsoid are given by

$$\mathbf{I}_i = \frac{m_i}{2\kappa} \begin{pmatrix} B_i^2 + C_i^2 & 0 & 0 \\ 0 & C_i^2 + A_i^2 & 0 \\ 0 & 0 & A_i^2 + B_i^2 \end{pmatrix} \tag{4}$$

which, for $\kappa = 5/2$, are the same principal moments of inertia of an ellipsoid of constant density. This is relevant for the estimation of the spin velocities, as we will see in Section 4.3.

2.1. Interaction potential

The evolution of the system is described by the Lagrangian function

$$\mathcal{L}(\mathbf{r}, \boldsymbol{\varphi}, \dot{\mathbf{r}}, \dot{\boldsymbol{\varphi}}) = \mathcal{K}_{\mathrm{T}} + \mathcal{K}_{\mathrm{R}} - \sum_{i=1}^{N-1} \sum_{j=i+1}^{N} \mathcal{U}_{ij}, \tag{5}$$

where $\mathcal{K}_{\mathrm{T}} = \sum_{i=1}^{N} m_i \dot{\mathbf{r}}_i^2/2$ is the translational kinetic energy, $\mathcal{K}_{\mathrm{R}} = \sum_{i=1}^{N} \boldsymbol{\omega}_i^{\mathrm{T}} \mathbf{I}_i \boldsymbol{\omega}_i/2$ is the rotational kinetic energy, and $\mathcal{U}_{ij}$ is the interaction potential. This latter is given by the sum of a gravitational attractive term $\mathcal{U}_{\mathrm{G}ij}$ and a contact repulsive term $\mathcal{U}_{\mathrm{C}ij}$, which avoids the penetration between the ellipsoids. In our approach, we consider only the gravitational monopole

$$\mathcal{U}_{\mathrm{G}ij} = -\frac{G m_i m_j}{|\mathbf{r}_i - \mathbf{r}_j|}, \tag{6}$$

where G is the gravitational constant, and define

$$\mathcal{U}_{\mathrm{C}ij} = \mathcal{U}_{0ij} \int_{-\infty}^{\infty} \mathrm{d}^3\mathbf{r}\, \rho_i(\mathbf{r}) \rho_j(\mathbf{r}), \tag{7}$$

[1] The Euler angles are defined such that θ represents the obliquity of a body spinning around its minor axis.

[2] Hereafter, a vector $\mathbf{s}$ will be assumed to be a column vector while $\mathbf{s}^{\mathrm{T}}$ will represent a row vector. Thus $\mathbf{s}^{\mathrm{T}}\mathbf{s} = \mathbf{s} \cdot \mathbf{s} = \mathbf{s}^2$ is the usual scalar product and $\mathbf{s}\mathbf{s}^{\mathrm{T}} = \mathbf{s}\mathbf{s}\cdot$ is a projection matrix.

where $\mathcal{U}_{0ij}$ is a constant to be determined. The potential $\mathcal{U}_{Cij}$ is large when the ellipsoids are close by, and rapidly goes to zero as they get apart. Explicitly we have

$$\mathcal{U}_{Cij} = \mathcal{U}_{0ij}\rho_{0i}\rho_{0j}\exp\bigl(-\kappa(\mathbf{r}_i-\mathbf{r}_j)^{\mathrm{T}}\mathbf{Q}_{ij}(\mathbf{r}_i-\mathbf{r}_j)\bigr) \times \int_{-\infty}^{\infty} \mathrm{d}^3\mathbf{r}\exp\bigl(-\kappa(\mathbf{r}-\mathbf{r}_{ij})^{\mathrm{T}}(\boldsymbol{\Lambda}_i+\boldsymbol{\Lambda}_j)(\mathbf{r}-\mathbf{r}_{ij})\bigr), \tag{8}$$

where

$$\boldsymbol{\Lambda}_i = \mathbf{R}_i^{\mathrm{T}}\mathbf{E}_i\mathbf{R}_i,$$
$$\mathbf{r}_{ij} = (\boldsymbol{\Lambda}_i+\boldsymbol{\Lambda}_j)^{-1}(\boldsymbol{\Lambda}_i\mathbf{r}_i+\boldsymbol{\Lambda}_j\mathbf{r}_j), \tag{9}$$

and $\mathbf{Q}_{ij}$ is the totally symmetric matrix defined by $\mathbf{Q}_{ij} = \boldsymbol{\Lambda}_i(\boldsymbol{\Lambda}_i+\boldsymbol{\Lambda}_j)^{-1}\boldsymbol{\Lambda}_j = \mathbf{Q}_{ji}$.

The integral in Eq. (8) can be easily evaluated to get

$$\mathcal{U}_{Cij} = \mathcal{U}_{0ij}\rho_{0i}\rho_{0j}\exp\bigl(-\kappa(\mathbf{r}_i-\mathbf{r}_j)^{\mathrm{T}}\mathbf{Q}_{ij}(\mathbf{r}_i-\mathbf{r}_j)\bigr) \times \sqrt{\frac{\pi^3}{\kappa^3}}\bigl[\det|\boldsymbol{\Lambda}_i+\boldsymbol{\Lambda}_j|\bigr]^{-1/2}. \tag{10}$$

The values of $\mathcal{U}_{0ij}$ and κ are determined only once by requiring that

(i) the mutual potential $\mathcal{U}_{Cij}+\mathcal{U}_{Gij}$ has a minimum $\mathcal{U}_{ij}^{\min}$ when the ellipsoids' surfaces are in contact;
(ii) this minimum is of the order of the mutual gravitational potential, more precisely

$$f \leqslant \frac{\mathcal{U}_{ij}^{\min}}{\mathcal{U}_{Gij}} < 1, \quad \text{with } f \gg 0.$$

Assuming spherical fragments of radius R_i, R_j, the above conditions lead to

$$\kappa = \frac{1}{2(1-f)} > \frac{3}{2},$$
$$\mathcal{U}_{0ij} = \frac{G\pi^{3/2}}{2}(R_i+R_j)^2\frac{\exp(\kappa\lambda_{ij})}{(\kappa\lambda_{ij})^{5/2}}, \tag{11}$$

where

$$\lambda_{ij} = \frac{(R_i+R_j)^2}{R_i^2+R_j^2} \tag{12}$$

is such that $1 < \lambda_{ij} \leqslant 2$. In the case of ellipsoidal bodies, the values of κ and $\mathcal{U}_{0ij}$ can be still determined by Eqs. (11)–(12) using the "equivalent radius" $R_i = (A_iB_iC_i)^{1/3}$. The shape of the interaction potential is shown in Fig. 1.

The value of κ (or f) in Eq. (11) is a free parameter of the model. An appropriate value of κ may be fixed by requiring that during a high-velocity collision between any pair of ellipsoids, the kinetic energy of the impacting body is much smaller than the maximum of the mutual potential barrier (see Fig. 1). In this way, we avoid penetration between the bodies. In practice, this is done by considering the pair k, l having the smallest amplitude in their contact mutual potential (Eq. (10)), and constraining this amplitude in such a way

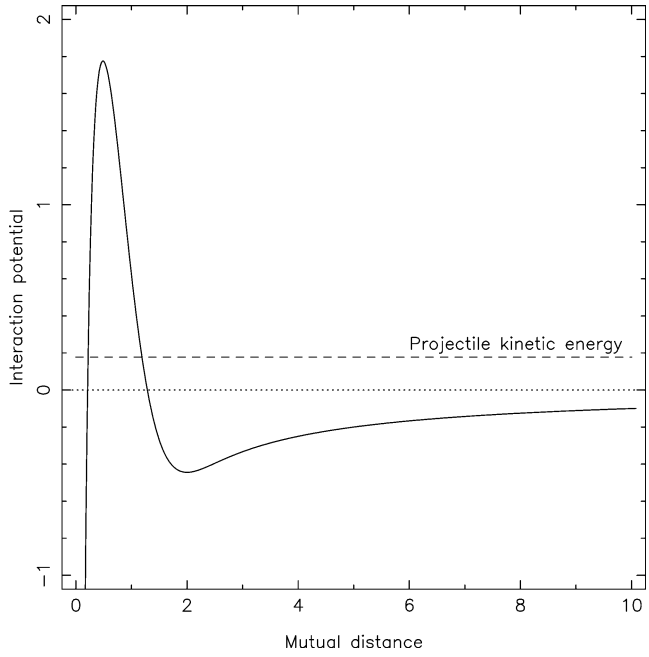

Fig. 1. Interaction potential $\mathcal{U}_{ij}$ in dependence of the mutual distance $|\mathbf{r}_i-\mathbf{r}_j|$. The minimum is approximately located at the point where the centers of mass of the ellipsoids are separated by a distance R_i+R_j (see text). The maximum of the potential barrier is about ten times larger than the kinetic energy of a typical projectile.

that

$$\mathcal{U}_{0kl}\rho_{0k}\rho_{0l}\sqrt{\frac{\pi^3}{\kappa^3}}\bigl[\det|\boldsymbol{\Lambda}_k+\boldsymbol{\Lambda}_l|\bigr]^{-1/2} = \beta\mathcal{K}, \tag{13}$$

where $\mathcal{K}$ is a prescribed kinetic energy, as large as possible, and $\beta \sim 10$.

Equation (13) has to be solved for κ using the largest possible value of m_l and the smallest possible value of m_k. If we assume spherical bodies and choose $\mathcal{K} = m_l\mathbf{v}^2/2$—for a prescribed value of the relative velocity $\mathbf{v}$—, we may write Eq. (13) as

$$\frac{\exp(\kappa\lambda_{kl})}{\kappa\lambda_{kl}} = \beta\mathbf{v}^2\frac{R_k+R_l}{Gm_k}, \tag{14}$$

which may be easily solved by Newton's method. Note that, since $\kappa > 3/2$, the above relation constrains the prescribed impact velocities to $\mathbf{v}^2 > 0.3Gm_k/(R_k+R_l)$.

The use of triaxial ellipsoids, and the dependence of the contact potential on the fragments' shapes, are essential for the description of the attitudes and spins of the fragments. Otherwise no spin–spin interactions would take place and only the translational degrees of freedom would participate in the dynamics.[3] However, even if the bodies have ellip-

[3] Actually, for two spherical bodies of radius R_i, R_j we have

$$(\mathbf{r}_i-\mathbf{r}_j)^{\mathrm{T}}\mathbf{Q}_{ij}(\mathbf{r}_i-\mathbf{r}_j) = (\mathbf{r}_i-\mathbf{r}_j)^2/\bigl(R_i^2+R_j^2\bigr),$$
$$\det|\boldsymbol{\Lambda}_i+\boldsymbol{\Lambda}_j| = \bigl(R_i^2+R_j^2\bigr)^3/\bigl(R_i^6R_j^6\bigr),$$

and the interaction potential does not depend on the Euler angles.

soidal shape, the multipole gravitational interactions among them are neglected for the sake of simplicity. We may argue that the effects of quadrupole or higher multipole interactions have no appreciable influence on the dynamics during short time scale collisional processes; thus they may be neglected for the purpose of the present study. On the other hand, we should expect that multipole interactions play a significant role on the long term dynamics, contributing to change the spin rates and tumbling states of the bodies, as pointed out by Scheeres et al. (2000). Therefore, multipole interactions should be taken into account for study long time scale processes like gravitational re-accumulation or tidal disruption.

2.2. Quaternions

The use of Euler angles to follow the evolution of the attitude of a rigid body presents a major shortcoming: the equations of motion *become singular* when the angle θ, i.e., the obliquity of the body, goes to zero. This is because, for $\theta = 0$, the other angles ϕ, ψ cannot be determined as independent quantities, since only the sum $\phi + \psi$ is defined. This limitation can be overcome by substituting the Euler angles with an adequate set of regular variables. These regular variables are known as "quaternions" (Whittaker, 1959).

Quaternions are a set of 4-vectors, $\bar{\mathbf{q}} = (\mathbf{q}, q)$, with $\mathbf{q}$ being a 3-vector and q a scalar, for which the following binary products are defined:

$$\bar{\mathbf{q}}_1 \cdot \bar{\mathbf{q}}_2 = \mathbf{q}_1 \cdot \mathbf{q}_2 + q_1 q_2, \tag{15}$$

$$\bar{\mathbf{q}}_1 \times \bar{\mathbf{q}}_2 = (q_1\mathbf{q}_2 + q_2\mathbf{q}_1 - \mathbf{q}_1 \times \mathbf{q}_2,\ q_1 q_2 - \mathbf{q}_1 \cdot \mathbf{q}_2). \tag{16}$$

Under the product Eq. (16) a set of uni-modulus quaternions ($\bar{\mathbf{q}}^2 = 1$) form a group which is isomorphic to the group $SU(2)$ of rotations in the unit sphere, hence to the group $O(3)$. Therefore, a set of uni-modulus quaternions can be used as a representation of the group of 3D rotations. If we define the quaternion $\bar{\mathbf{r}} = (\mathbf{r}, 0)$, the rotation of the vector $\mathbf{r}$ by an angle χ around the unit vector $\mathbf{n}$ may be expressed as

$$\bar{\mathbf{r}}' = \bar{\mathbf{q}}^{-1} \times \bar{\mathbf{r}} \times \bar{\mathbf{q}}, \tag{17}$$

where

$$\bar{\mathbf{q}} = \left(\sin\frac{\chi}{2}\mathbf{n}, \cos\frac{\chi}{2}\right),$$
$$\bar{\mathbf{q}}^{-1} = \left(-\sin\frac{\chi}{2}\mathbf{n}, \cos\frac{\chi}{2}\right). \tag{18}$$

Hereafter, we will omit the "bars" and will denote the quaternion associated to the ith ellipsoid simply as $\mathbf{q}_i = (\alpha_i, \beta_i, \gamma_i, \delta_i)$. The components of $\mathbf{q}_i$ are defined in terms of the Euler angles as follows:

$$\alpha_i = \sin\frac{\theta_i}{2}\cos\frac{\phi_i - \psi_i}{2}, \qquad \beta_i = \sin\frac{\theta_i}{2}\sin\frac{\phi_i - \psi_i}{2},$$
$$\gamma_i = \cos\frac{\theta_i}{2}\sin\frac{\phi_i + \psi_i}{2}, \qquad \delta_i = \cos\frac{\theta_i}{2}\cos\frac{\phi_i + \psi_i}{2}, \tag{19}$$

and this definition clearly avoids the problem with the indetermination of ϕ and ψ when $\theta = 0$. Note that we are substituting the use of *three* Euler angles by *four* quaternion's components satisfying the constraint

$$\mathbf{q}_i^2 = \alpha_i^2 + \beta_i^2 + \gamma_i^2 + \delta_i^2 = 1. \tag{20}$$

We may now write the rotation matrix $\mathbf{R}_i$ appearing in Eq. (2) in terms of the quaternion's components. This takes the form

$$\mathbf{R}_i = 2\begin{pmatrix} \alpha_i^2 + \delta_i^2 - \frac{1}{2} & \alpha_i\beta_i + \gamma_i\delta_i & \alpha_i\gamma_i - \beta_i\delta_i \\ \alpha_i\beta_i - \gamma_i\delta_i & \beta_i^2 + \delta_i^2 - \frac{1}{2} & \beta_i\gamma_i + \alpha_i\delta_i \\ \alpha_i\gamma_i + \beta_i\delta_i & \beta_i\gamma_i - \alpha_i\delta_i & \gamma_i^2 + \delta_i^2 - \frac{1}{2} \end{pmatrix} \tag{21}$$

and, as expected, $\mathbf{R}_i^{-1}\mathbf{R}_i = \mathbf{R}_i^{\mathrm{T}}\mathbf{R}_i = \mathbf{1}$. As we see, the rotation matrix is now written in terms of a bilinear form of the quaternion components. This is another advantage of the use of quaternions in numerical procedures, since the attitude of a rigid body is no longer described in terms of time-consuming trigonometric functions.

Taking the time derivative of Eq. (21) and using the fact that

$$\mathbf{q}_i \cdot \dot{\mathbf{q}}_i = 0 \tag{22}$$

we may write the spin of a body (Eq. (1)) as:

$$\begin{pmatrix} \boldsymbol{\omega}_i \\ 0 \end{pmatrix} = 2\mathbf{W}_i\dot{\mathbf{q}}_i, \tag{23}$$

where

$$\mathbf{W}_i = \begin{pmatrix} \delta_i & \gamma_i & -\beta_i & -\alpha_i \\ -\gamma_i & \delta_i & \alpha_i & -\beta_i \\ \beta_i & -\alpha_i & \delta_i & -\gamma_i \\ \alpha_i & \beta_i & \gamma_i & \delta_i \end{pmatrix}, \tag{24}$$

and again $\mathbf{W}_i^{-1}\mathbf{W}_i = \mathbf{W}_i^{\mathrm{T}}\mathbf{W}_i = \mathbf{1}$. As a consequence, the rotational kinetic energy of the body takes the form

$$\mathcal{K}_{\mathrm{R}} = \frac{1}{2}\dot{\mathbf{q}}_i^{\mathrm{T}}\mathbf{M}_i\dot{\mathbf{q}}_i, \tag{25}$$

where $\mathbf{M}_i = 4\mathbf{W}_i^{\mathrm{T}}\tilde{\mathbf{I}}_i\mathbf{W}_i$, and $\tilde{\mathbf{I}}_i$ is the 4×4 diagonal matrix

$$\tilde{\mathbf{I}}_i = \begin{pmatrix} \mathbf{I}_i & \mathbf{0} \\ \mathbf{0} & \mathrm{Tr}(\mathbf{I}_i) \end{pmatrix} \tag{26}$$

obtained from Eq. (4).

2.3. Equations of motion

With the introduction of the quaternions, the Lagrangian of the system can be expressed as

$$\begin{aligned} \mathcal{L}(\mathbf{r}, \mathbf{q}, \dot{\mathbf{r}}, \dot{\mathbf{q}}) = &\sum_{i=1}^{N}\frac{1}{2}m_i\dot{\mathbf{r}}_i^2 + \sum_{i=1}^{N}\frac{1}{2}\dot{\mathbf{q}}_i^{\mathrm{T}}\mathbf{M}_i(\mathbf{q}_i)\dot{\mathbf{q}}_i \\ &- \sum_{i=1}^{N-1}\sum_{j=i+1}^{N}\mathcal{U}_{\mathrm{C}ij}\left(|\mathbf{r}_i - \mathbf{r}_j|, \mathbf{q}_i, \mathbf{q}_j\right) \\ &- \sum_{i=1}^{N-1}\sum_{j=i+1}^{N}\mathcal{U}_{\mathrm{G}ij}\left(|\mathbf{r}_i - \mathbf{r}_j|\right). \end{aligned} \tag{27}$$

The conjugate momenta are

$$\mathbf{u}_i = \frac{\partial \mathcal{L}}{\partial \dot{\mathbf{r}}_i} = m_i \dot{\mathbf{r}}_i, \qquad \mathbf{p}_i = \frac{\partial \mathcal{L}}{\partial \dot{\mathbf{q}}_i} = \mathbf{M}_i \dot{\mathbf{q}}_i, \tag{28}$$

and the equations of motion take the form

$$\dot{\mathbf{u}}_i = \frac{\partial \mathcal{L}}{\partial \mathbf{r}_i}, \qquad \dot{\mathbf{p}}_i = \frac{\partial \mathcal{L}}{\partial \mathbf{q}_i}, \tag{29}$$

where the symbols $\partial/\partial \mathbf{r}_i, \partial/\partial \mathbf{q}_i$ represent gradients. The computation of the second members is relatively straightforward.[4]

Although the use of quaternions avoids the occurrence of singularities in the equations of motion, they introduce an additional complication: we have now $7N$ second-order differential equations to solve instead of the original $6N$ equations. It is clear that N of these equations can be eliminated using the constraints Eqs. (20) and (22). However, the direct elimination of one component of the quaternion is found to be undesirable, because the remaining equations of motions become much more complicated, containing non-linear relations among the other three components. Moreover, if we use only three components of the quaternion, the resulting equations of motion become always singular at some point, just like the equations for the Euler angles, hence destroying the main advantage of the use of quaternions.

In view of this, we will keep all the four components of the quaternions in our calculations, and will incorporate the constraints through the method of Lagrange multipliers. Since the equations for $\dot{\mathbf{u}}_i$ are not affected by this procedure, we will concentrate only in the equations for $\dot{\mathbf{p}}_i$. The standard procedure is to use Eq. (20) to define the "effective" Lagrangian

$$\widetilde{\mathcal{L}} = \mathcal{L} - \sum_{i=1}^{N} \frac{1}{2}\big(\mathbf{q}_i^2 - 1\big)\lambda_i(t), \tag{30}$$

where the Lagrange multipliers λ_i are scalar functions of time. The constraint Eq. (20) leads to

$$\lambda_i(t) = \mathbf{q}_i \cdot \frac{\partial \mathcal{L}}{\partial \mathbf{q}_i} - \mathbf{q}_i \cdot \dot{\mathbf{p}}_i. \tag{31}$$

Therefore, the equations of motion are re-written as

$$\dot{\mathbf{p}}_i = \frac{\partial \widetilde{\mathcal{L}}}{\partial \mathbf{q}_i} = \frac{\partial \mathcal{L}}{\partial \mathbf{q}_i} - \mathbf{q}_i \lambda_i(t), \tag{32}$$

and substituting Eq. (31) in Eq. (32) we get

$$\{\mathbf{1} - \mathbf{q}_i \mathbf{q}_i \cdot\}\dot{\mathbf{p}}_i = \{\mathbf{1} - \mathbf{q}_i \mathbf{q}_i \cdot\}\frac{\partial \mathcal{L}}{\partial \mathbf{q}_i}. \tag{33}$$

The operator $\{\mathbf{1} - \mathbf{q}_i \mathbf{q}_i \cdot\} \equiv \mathbf{q}^2 - \mathbf{q}\mathbf{q}^{\mathrm{T}}$ is a "4×4-projector" such that $\{\mathbf{1} - \mathbf{q}_i \mathbf{q}_i \cdot\}\mathbf{q}_i = 0$, which means that, as expected, the components of $\mathbf{q}_i$ are not linearly independent.

Since, for a given $\mathbf{q}_i$, one component of the vectorial equation (33) is linearly dependent on the other three, we need an additional equation to replace it. Combining Eq. (22) with (28) we have

$$\mathbf{q}_i \cdot \dot{\mathbf{q}}_i \equiv \mathbf{q}_i^{\mathrm{T}} \mathbf{M}_i^{-1} \mathbf{p}_i = 0, \tag{34}$$

and taking the time derivative and re-arranging terms, we arrive to the scalar equation

$$\mathbf{q}_i^{\mathrm{T}} \mathbf{M}_i^{-1} \dot{\mathbf{p}}_i = \mathbf{q}_i^{\mathrm{T}} \mathbf{M}_i^{-1} \dot{\mathbf{M}}_i \mathbf{M}_i^{-1} \mathbf{p}_i - \mathbf{p}_i^{\mathrm{T}} \mathbf{M}_i^{-2} \mathbf{p}_i, \tag{35}$$

where $\dot{\mathbf{M}}_i$ depends on $\dot{\mathbf{W}}_i = \dot{\mathbf{W}}(\dot{\mathbf{q}}_i)$, which is obtained by taking the time derivative of each coefficient of $\mathbf{W}_i$.

The procedure to advance the differential equations for a given $\mathbf{p}_i$ is to discard one component from the vectorial equation (33) and replace it with Eq. (35). Since Eq. (33) does not provide any information in the direction of $\mathbf{q}_i$, the best choice would be to replace the component that is precisely in the direction of $\mathbf{q}_i$, or at least, the component that has the largest scalar product with $\mathbf{q}_i$. In practice, this can be done by choosing the component of $\mathbf{q}_i$ which has the largest absolute value, and eliminating the equation corresponding to this component from Eq. (33). As a result, we get the following linear system of equations that has to be solved for $\dot{\mathbf{p}}_i$:

$$\begin{pmatrix} \{\mathbf{1} - \mathbf{q}_i \mathbf{q}_i \cdot\}^* \\ \mathbf{q}_i^{\mathrm{T}} \mathbf{M}_i^{-1} \end{pmatrix} \dot{\mathbf{p}}_i = \begin{pmatrix} \{\mathbf{1} - \mathbf{q}_i \mathbf{q}_i \cdot\}^* \partial \mathcal{L}/\partial \mathbf{q}_i \\ \mathbf{q}_i^{\mathrm{T}} \mathbf{M}_i^{-1} \dot{\mathbf{M}}_i \mathbf{M}_i^{-1} \mathbf{p}_i - \mathbf{p}_i^{\mathrm{T}} \mathbf{M}_i^{-2} \mathbf{p}_i \end{pmatrix}, \tag{36}$$

where $\{\mathbf{1} - \mathbf{q}_i \mathbf{q}_i \cdot\}^*$ represents the "3×4-projector" obtained from deleting the row of $\{\mathbf{1} - \mathbf{q}_i \mathbf{q}_i \cdot\}$ corresponding to the largest component of $\mathbf{q}_i$.

It is worth noting that Eqs. (29) and (36) describe the evolution of a conservative system that *preserves total energy and total linear and angular momenta*. Conservation of energy implies that the interaction between the ellipsoids occur in a regime of total elasticity. This is not the case for real systems, where we should expect that energy dissipates (for example, in the form of heat) due to mutual collisions and/or friction. We will see in the next section how we may take into account these effects.

2.4. Dissipation function

In order to incorporate dissipation of energy in our model we introduce a dissipation function $\mathcal{F}(\mathbf{r}, \mathbf{q}, \dot{\mathbf{r}}, \dot{\mathbf{q}})$ such that the equations of motion take the form

$$\dot{\mathbf{u}}_i = \frac{\partial \mathcal{L}}{\partial \mathbf{r}_i} + \frac{\partial \mathcal{F}}{\partial \dot{\mathbf{r}}_i}, \qquad \dot{\mathbf{p}}_i = \frac{\partial \mathcal{L}}{\partial \mathbf{q}_i} - \mathbf{q}_i \lambda_i(t) + \frac{\partial \mathcal{F}}{\partial \dot{\mathbf{q}}_i}. \tag{37}$$

[4] Note that, to determine $\dot{\mathbf{p}}$, it is necessary to compute the gradient of $\det|\boldsymbol{\Lambda}_i + \boldsymbol{\Lambda}_j|$. This may be obtained from the definition

$$\frac{\partial \det|\boldsymbol{\Lambda}(q)|}{\partial q} = \lim_{\delta q \to 0} \frac{\det|\boldsymbol{\Lambda}(q+\delta q)| - \det|\boldsymbol{\Lambda}(q)|}{\delta q}.$$

Using the fact that $\boldsymbol{\Lambda}(q+\delta q) \simeq \boldsymbol{\Lambda}(q) + \frac{\partial \boldsymbol{\Lambda}}{\partial q}\delta q$, and that $\det|1 + \boldsymbol{\Lambda}\delta q| \simeq 1 + \mathrm{Tr}(\boldsymbol{\Lambda})\delta q$, the result is

$$\frac{\partial \det|\boldsymbol{\Lambda}_i + \boldsymbol{\Lambda}_j|}{\partial \mathbf{q}_i} = \det|\boldsymbol{\Lambda}_i + \boldsymbol{\Lambda}_j| \,\mathrm{Tr}\Big((\boldsymbol{\Lambda}_i + \boldsymbol{\Lambda}_j)^{-1} \frac{\partial \boldsymbol{\Lambda}_i}{\partial \mathbf{q}_i}\Big).$$

We will require that this function be:

(i) bi-quadratic in $\dot{\mathbf{r}}$ and $\dot{\mathbf{q}}$, and
(ii) negative definite.

Under these assumptions, it is straightforward to show that $\mathrm{d}\mathcal{H}/\mathrm{d}t = 2\mathcal{F} < 0$, where $\mathcal{H}$ is the total energy (Hamiltonian) of the system. $\mathcal{F}$ is usually called the "Rayleigh dissipation function."

We would also like to introduce the dissipation mechanism among the interacting ellipsoids in such a way that the dissipation only occurs when their surfaces are in contact, but it vanishes as soon as they reach a collective rigid body motion. We start by considering two ellipsoidal bodies, i and j, that partially overlap each other, and a point of coordinate $\mathbf{r}$ lying in the overlapping region. If $\mathbf{s}^{(i)}$ represents the coordinate of this point in the reference system fixed to ellipsoid i (i.e., aligned with its principal axes), we may write $\mathbf{r} = \mathbf{r}_i + \mathbf{R}_i^{\mathrm{T}}\mathbf{s}^{(i)}$, that is, $\mathbf{s}^{(i)} = \mathbf{R}_i(\mathbf{r} - \mathbf{r}_i)$. In the same way, if $\mathbf{s}^{(j)}$ is the coordinate of the point in the reference system fixed to ellipsoid j, we have $\mathbf{s}^{(j)} = \mathbf{R}_j(\mathbf{r} - \mathbf{r}_j)$. Now, the velocity of the point in terms of the motion of ellipsoid i is

$$\dot{\mathbf{r}}^{(i)} = \dot{\mathbf{r}}_i + \dot{\mathbf{R}}_i^{\mathrm{T}}\mathbf{s}^{(i)}, \tag{38}$$

where $\dot{\mathbf{R}}_i = \dot{\mathbf{R}}(\mathbf{q}_i, \dot{\mathbf{q}}_i)$ is obtained by taking the time derivative of each coefficient of $\mathbf{R}_i$. In the same way, in terms of the motion of ellipsoid j, we have

$$\dot{\mathbf{r}}^{(j)} = \dot{\mathbf{r}}_j + \dot{\mathbf{R}}_j^{\mathrm{T}}\mathbf{s}^{(j)} \tag{39}$$

and the condition of rigid body motion holds if $\dot{\mathbf{r}}^{(i)} = \dot{\mathbf{r}}^{(j)}$ for all $\mathbf{r}$.

From the above considerations, a possible choice for the Rayleigh dissipation function (among others) would be $\mathcal{F} = \sum_{i=1}^{N-1}\sum_{j=i+1}^{N}\mathcal{F}_{ij}$ with

$$\mathcal{F}_{ij} = -\mathcal{F}_0\mathcal{U}_{0ij}\int_{-\infty}^{\infty}\mathrm{d}^3\mathbf{r}\,\rho_i(\mathbf{r})\rho_j(\mathbf{r})\left(\dot{\mathbf{r}}^{(i)} - \dot{\mathbf{r}}^{(j)}\right)^2. \tag{40}$$

We may note that $\dot{\mathbf{R}}$ is linear in $\dot{\mathbf{q}}$, thus, this choice of $\mathcal{F}_{ij}$ fulfills conditions (i) and (ii), is large only when the ellipsoids are in mutual contact, and vanishes for a collective rigid body motion. Since $\mathcal{F}$ is expressed in terms of the motion of a point, we will refer to it as the "point dissipation function." Explicitly, we get:

$$\begin{aligned}\mathcal{F}_{ij} = -\mathcal{F}_0\mathcal{U}_{\mathrm{C}ij}\Bigg\{&\frac{1}{2\kappa}\,\mathrm{Tr}\left(\boldsymbol{\Gamma}_{ij}^{\mathrm{T}}(\boldsymbol{\Lambda}_i + \boldsymbol{\Lambda}_j)^{-1}\boldsymbol{\Gamma}_{ij}\right)\\ &+\left[\dot{\mathbf{r}}_i - \dot{\mathbf{r}}_j + \dot{\mathbf{R}}_i^{\mathrm{T}}\mathbf{R}_i(\mathbf{r}_{ij} - \mathbf{r}_i)\right.\\ &\left.-\dot{\mathbf{R}}_j^{\mathrm{T}}\mathbf{R}_j(\mathbf{r}_{ij} - \mathbf{r}_j)\right]^2\Bigg\}\end{aligned} \tag{41}$$

where $\boldsymbol{\Lambda}_i$, $\boldsymbol{\Lambda}_j$ and $\mathbf{r}_{ij}$ are given by Eqs. (9), and $\boldsymbol{\Gamma}_{ij}$ is the anti-symmetric matrix defined by $\boldsymbol{\Gamma}_{ij} = \dot{\mathbf{R}}_i^{\mathrm{T}}\mathbf{R}_i - \dot{\mathbf{R}}_j^{\mathrm{T}}\mathbf{R}_j = -\boldsymbol{\Gamma}_{ji}$. The derivatives of $\mathcal{F}$ with respect to $\dot{\mathbf{r}}_i$ and $\dot{\mathbf{q}}_i$ are straightforward.

The coefficient $\mathcal{U}_{0ij}$ is given by Eq. (11), while the coefficient $\mathcal{F}_0$ may be arbitrarily chosen to achieve the desired dissipation. A large value of $\mathcal{F}_0$, for example, allows the perfect sticking of two colliding bodies. In this sense, *the dissipation function also acts as a cohesive force* that introduces some sort of mutual strength between the fragments in the rubble-pile. In practice, we fix $\mathcal{F}_0 \approx 1$. This choice seemed to be the most appropriate since, in all our examples of high velocity impacts, the fraction f_{KE} of kinetic energy that is transferred from the projectile to the fragments is between 1 and 10%, in good agreement with the values found in the literature, and we are able to reproduce the typical ejection velocities ($\sim 100\ \mathrm{m\,s^{-1}}$) predicted by hydrocodes.

Finally, we can show that the point dissipation function Eq. (41) only dissipates energy but does not modify other conservation laws, i.e., *the total linear and angular momenta of the system are preserved* (see Appendix A). Notwithstanding, we would like to stress that this is an arbitrary choice and there is no especial reason to require that a given dissipation function should preserve either linear or angular momentum. For example, our model is not accounting for the production of dust at the impact point during a collision, and we might expect that some fraction of momentum is carried out by this cloud of dust (see Paolicchi et al., 2003). In this case, neither linear nor angular momentum would be conserved. However, at variance with kinetic energy, we do not know how to calibrate this effect, so we prefer to keep a form of dissipation that preserves linear and angular momentum.

3. Numerical experiments

We perform a series of numerical experiments of collisional events with high-velocity projectiles impacting rubble-pile targets. In these calculations, we vary the different parameters of the system like the specific impact energy, the impact angle and the properties of the target, as explained in the following.

Each target consists of N monolithic ellipsoidal fragments following a power law cumulative size distribution $\propto D^{-2.5}$. All the fragments have the same shape, with their principal axes in the ratios $B_i/A_i = 0.7$ and $C_i/A_i = 0.5$, which are the approximate ratios usually inferred from asteroid light curves (e.g., Harris and Burns, 1979). The mean mass density of the fragments was set to $\bar{\rho} = 3\ \mathrm{g\,cm^{-3}}$ in all cases. Recall that $\bar{\rho}$ is related to the "peak" density in Eq. (2) through

$$\rho_{0i} = \frac{4}{3}\bar{\rho}_i\sqrt{\frac{\kappa^3}{\pi}}. \tag{42}$$

The fragments are initially oriented and distributed at random, with the largest one being at the center of the rubble-pile. We expect that this would be the natural result from a re-accumulation process, where the largest fragments aggregate first, leaving the smaller ones near the surface of the

Table 1
Properties of the different targets used in our numerical experiments

Target	N30	N100	N200
Total mass [10^{18} kg]	10.03	9.99	10.05
Effective radius [km]	92.76	92.64	92.82
Apparent radius [km]	107.44	107.43	110.10
Effective density [g cm^{-3}]	3.00	3.00	3.00
Apparent density [g cm^{-3}]	1.93	1.92	1.80
Porosity	0.36	0.36	0.40
Major radius of largest fragment [km]	90.51	84.85	83.43
Equivalent radius of largest fragment [km]	64.00	60.00	59.00
Major radius of smallest fragment [km]	22.62	14.14	9.89
Equivalent radius of smallest fragment [km]	16.00	10.00	7.00

The effective radius is computed from the sum of the volumes of the individual fragments, while the apparent radius is the average geometric radius of the target. This latter is computed from the distances between the edges of the ensemble of fragments along the directions x, y, z. The porosity is calculated from the definition: $1 -$ apparent density / effective density.

rubble-pile. To mount such configurations, we use a Montecarlo code that generates a random distribution of fragments within a given volume. This volume is not much larger than the sum of the fragments' volumes, but it is large enough as to guarantee that initially the ellipsoids are not in mutual contact. In this configuration, the central ellipsoid is given an initial spin, Ω, around the z axis in the fixed coordinate system. The remaining ellipsoids are given an initial velocity in the x, y plane such that they all have the same angular velocity, Ω, around the center of mass of the system. These initial conditions are then evolved, including the effect of dissipation, until the ellipsoids re-accumulate and reach a collective nearly-rigid body motion. In this way, we end up with a rubble pile structure close to a figure of equilibrium and spinning around the z axis with an angular velocity $\sim \Omega$. Note that due to the particular setup of the parameters of the mutual potential $\mathcal{U}_{ij}$ (Eq. (11)), the ellipsoids may slightly overlap between them, but this overlap is just geometrical and does not affect the dynamics.

We setup different target configurations with $N = 30, 100$ or 200 fragments, in such a way that all the targets has approximately the same total mass $M \simeq 10^{19}$ kg. The targets are also initially rotating with periods $\tau = 4$ or 12 h. Table 1 summarizes some properties of the different targets used in our calculations.

The projectiles are represented by a single ellipsoidal body, with the same mass density and the same axis ratios as the target's fragments. We use three different projectiles, hereafter named P1, P2, and P3. Each projectile initially moves in the y, z plane toward the center of mass of the target with relative velocity $|\mathbf{v}_p| = 5$ km s^{-1}. The trajectory forms an angle ζ with the rotational axis of the target, that is set to $\zeta = 0°$, 45° or 90°. The projectiles have initially random attitude and zero spin. Table 2 summarizes some of the properties of these projectiles.

We may expect that during these high velocity impacts several fragments in the target were actually shattered and broken up, while in our numerical examples the different fragments are considered unbreakable. In principle, this is not an intrinsic limitation of the model, because the dissipation function (Eq. (41)) acts as a glue between the fragments. Thus, the breakup of a single fragment may be described in terms of the "breakup" of a collection of smaller glued fragments.[5] In this way, we may assume that we are not propagating the cracks during the impact—the shattering is already present in the target—, but simply partitioning the energy and angular momentum among the fragments.

Table 2
Properties of the projectiles used in our numerical experiments

Projectile	P1	P2	P3
Mass [10^{18} kg]	0.036	0.120	0.284
Major radius [km]	20.00	30.00	40.00
Equivalent radius [km]	14.14	21.21	28.28
Specific energy of impact [10^9 erg g^{-1}]	0.44	1.49	3.54

The specific energy of the impact is computed as: $Q = 0.5 m_p \mathbf{v}_p^2 / M$.

All the examples span 10 000 s. In all cases, the impact occurs at $t \simeq 80$–100 s. The equations of motion (Eq. (37)) are integrated in double precision using a Bulirsch–Stoer algorithm (Press et al., 1997). Positions and velocities are referred to the center of mass of the system. At each step of the integration, the linear equations (36) are solved through LU decomposition. The tolerance error for the solution of Bulirsch–Stoer routine is set to 10^{-8}–10^{-9}. This tolerance is rather small for this kind of integrator, but a more stringent value substantially increases the computational time. This is because the step size needs to be very small in order to resolve the motion when the ellipsoids are in mutual contact. Indeed, when a pair of ellipsoids fall deep into the potential basin of Fig. 1, their mutual distance rapidly oscillates, with a typical period of a few seconds or even less, and the step size is drastically reduced by the integrator. This problem disappears as soon as the ellipsoids get apart. A typical integration of 200 fragments requires about 15 hours of CPU on a Pentium 4 processor.

Finally, we check in our calculations for the conservation of energy and momenta. When dissipation is turned off, these quantities are preserved within the tolerance error used for the Bulirsch–Stoer propagator. With dissipation turned on, linear and angular momentum are still preserved within the same precision and, as expected, the energy decreases as $H(T) = H_0 + 2\int_0^T F \, \mathrm{d}t$.

4. Results

We concentrate our analysis on the behavior of some quantities that characterize the collisions and allow us to evaluate the performance of our model. Particular emphasis

[5] Of course this approach is limited by the resolution of the model, and would not be valid if the single fragment is likely to be pulverized.

is put on the behavior of the energy and angular momentum, as well as the ejection velocity field. The main capabilities of the model are especially exploited by analyzing the spin and attitude distributions of the fragments after the impacts.

From most results we can extract a qualitative tendency of the observables in the different numerical examples, and there are also some significant quantitative differences. All the results we present in the following refer to the dynamical state of the system *a few minutes after the impact*. In most cases we do not observe significant variations of these results over our integration time span. For example, the attitude and spin distributions are basically the same a few seconds after the impact than a few hours later (see Section 4.3). In our examples, some fragments ended in mutual escaping trajectories, while others remained bounded (see Section 4.2). Therefore, we may expect that these fragments will re-accumulate over the time-scales longer than our integration time span.

4.1. Energy partition and angular momentum

Figure 2a shows the energy partition during a typical collision between target N200 and projectile P2. At the moment of the impact ($t \simeq 80$ s) the projectile loses almost all its kinetic energy, which is mostly transferred to the kinetic energy of the fragments causing the peak in the dashed curve. However, during the collision there is a net loss of total energy due to dissipation (Eq. (41)), and a few seconds after the impact the fragments lose most of the energy they gained. Even if the final kinetic energy is always larger than the initial one, it only represents a small fraction of the projectile's kinetic energy. In all the examples, this fraction is between 1–5%, in good agreement with the typical limits of the anelasticity parameter f_{KE} usually found in the literature. Figure 2a also shows that most of the final kinetic energy goes to the translational motion, while only a small fraction—between 10–20%—remains in the rotational energy of the fragments. As we already mentioned, in all the examples the variation of total linear and angular momenta is within the tolerance error of the propagator (Fig. 2b) during the whole integration time span.

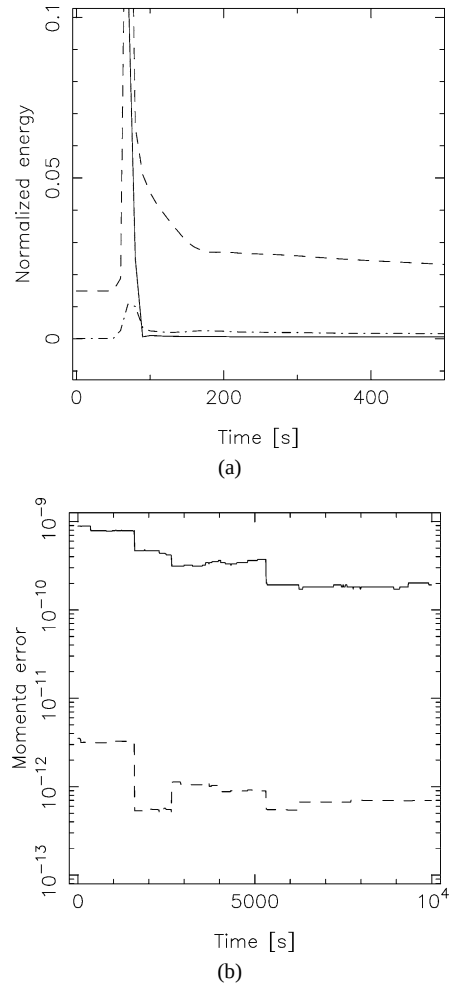

Fig. 2. (a) Energy partition during a collision between target N200 and projectile P2: kinetic energy of projectile (solid line), total—translational + rotational—kinetic energy of fragments (dashed line), rotational kinetic energy of fragments (dotted-dashed line). All energies are normalized to the initial value of the projectile's kinetic energy. The target is initially rotating with a period of 4 h, and the projectile impacts at an angle $\zeta = 45°$. (b) Variation of total angular momentum (solid line) and total linear momentum (dashed line) during the integration time span.

4.2. Ejection velocities

Ejection velocities of the fragments are computed as the difference between the post-impact velocity (at $t = 400$ s) and the pre-impact velocity (at $t = 0$). Analyzing these ejection velocities in the different examples, we find a systematic dependence on the number of fragments in the target: the smaller the number of fragments the smaller the average ejection velocity. This result is expected since the fragments from target N30 are larger than those from target N200 (see Table 1). Typical ejection velocities are roughly about 0.01–0.05% of the projectile velocity, but for the smallest fragments they may range between 0.004–0.2%. In all the examples, we observe that only small fragments are ejected at the impact point, while the largest ones tend to be ejected at the antipodal point. This effect is more noticeable for impacts onto targets with few fragments.

There is also a systematic dependence of the post-impact velocity field with the angle of impact. In all cases the field is aligned with the direction of the impact, but this alignment is more prominent when the impact occur along the z axis (recall that the rubble-pile is rotating around this axis). This is shown in Figs. 3a, 3b for a collision with projectile P2 impacting at an angle $\zeta = 0°$. When the impact occurs over the target's equator ($\zeta = 90°$), the alignment is not so prominent and there are more fragments ejected in the direction perpendicular to the impact direction, as shown in Figs. 3c, 3d.

In Fig. 4 we present the distribution of ejection velocities in dependence of the fragments' size for three different impact energies. The data may be fit by a power law rela-

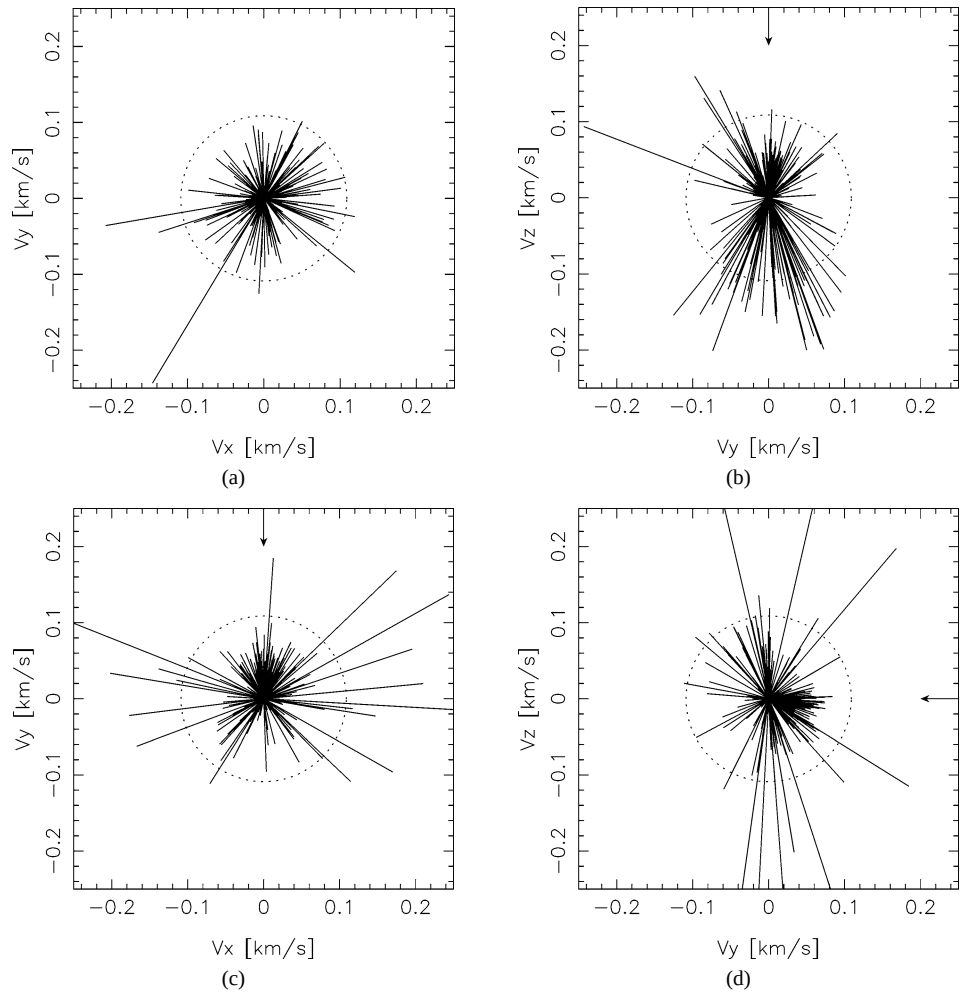

Fig. 3. Post-impact velocity field (300 s after the impact) in the v_x, v_y- and v_y, v_z-planes. Velocities are referred to the barycenter of the target. The results correspond to target N200, rotating with period of 12 h, and impacted by projectile P2. The dotted circle is the escape velocity limit. (a), (b) Impact with angle $\zeta = 0°$. (c), (d) Impact with angle $\zeta = 90°$. The impact direction is indicated by the arrows.

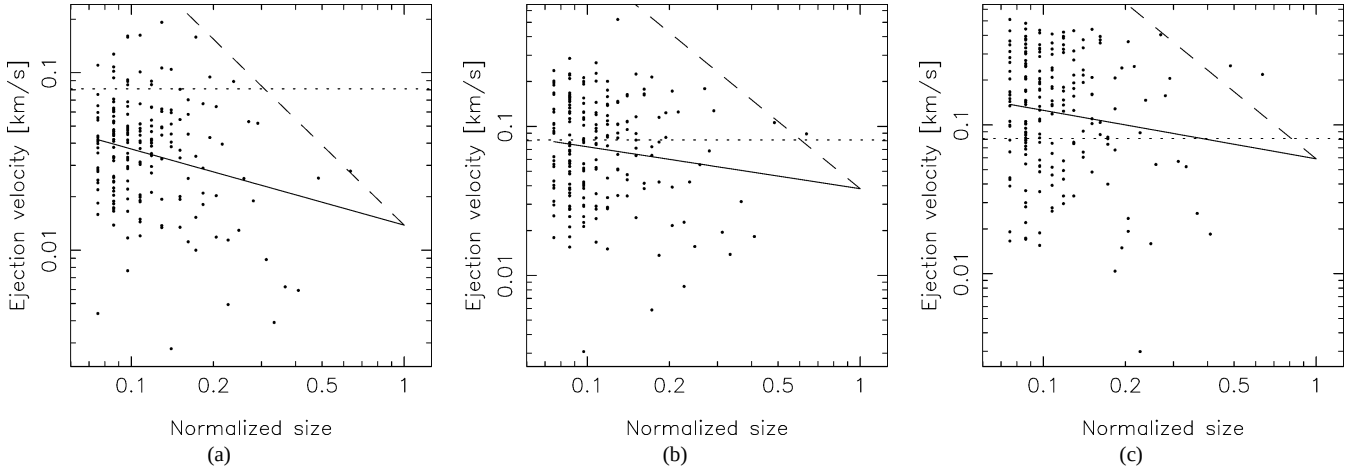

Fig. 4. Ejection velocity vs. fragments' size (normalized to the size of the parent body), 300 s after the impact. The results correspond to target N200, rotating with period 4 h, and impacted with an angle $\zeta = 45°$ by projectile P1 (a), P2 (b), and P3 (c). The dotted horizontal line indicates the ejection velocity limit for escape the parent body. The solid line is the power law best fit with exponent -0.42 (a), -0.28 (b), and -0.32 (c). The dashed line is the theoretical power law with exponent $-3/2$.

tionship (solid line), although there is a large dispersion of ejection velocities especially among the smaller fragments. In all our numerical examples, the exponent of this power law is between -0.10 and -0.50. These values are far away from the -1.5 exponent expected from the hypothesis of equipartition of kinetic energy (e.g., Cellino et al., 1999). Actually, this theoretical curve (dashed line) appears to be the upper boundary of the distributions.

From Fig. 4 it is evident that the collisions with projectile P1 do not generate sufficiently large ejection velocities to escape the parent body,[6] and most fragments start to re-accumulate very soon after disruption. Collisions with projectile P2 can also lead to the re-accumulation of several fragments, but this happens only over time scales of several hours. Finally, a large number of fragments is dispersed during collisions with projectile P3 and do not re-accumulate.

In order to estimate the amount of mass dispersed after the impacts, we compute the post-impact kinetic energy, $\mathcal{K}_i$, of each fragment, and assume that the fragment is in escaping trajectory if $\mathcal{K}_i \geqslant |\mathcal{U}_i^{\rm bind}|$, where

$$\mathcal{U}_i^{\rm bind} = -\sum_{j\neq i} \frac{G m_i m_j}{|\mathbf{r}_i - \mathbf{r}_j|} \tag{43}$$

is the gravitational binding energy of the fragment. The results for the three different impact energies used in our calculations are shown in Fig. 5. The fraction of mass that remains bounded after the impact varies almost linearly with the impact energy Q. The catastrophic threshold, for which 50% of the target mass is dispersed, is about $Q_{\rm D}^* = 2.6 \times 10^9$ erg g^{-1}. This is in good agreement with the values expected from typical scaling laws in the gravity dominated regime. For example, the catastrophic threshold estimated by Benz and Asphaug (1999) is about 2.68–4.49 $\times 10^9$ erg g^{-1} for our typical target size. Smaller values are predicted by Love and Ahrens (1996), 2.1×10^9 erg g^{-1}, and by Davis et al. (1995), 1.8×10^9 erg g^{-1}.

The dispersion observed in the fraction of surviving mass is somehow related to the initial rotation of the target. For targets rotating with a period of 4 h, the amount of mass dispersed after the impact is larger than for those initially rotating with 12 h period. This may be indicating that the rotational state of the target, which is not always accounted for in the SPH simulations, may play a relevant role in constraining the aggregation of fragments after a catastrophic collision.

[6] The escape velocity is computed according to Petit and Farinella (1993) as:

$$v_{\rm esc}^2 = 1.64 G M / R_{\rm eff}$$

where M and $R_{\rm eff}$ are the total mass and effective radius of the target, and G is the gravitational constant. This gives a value of ~ 109 m s^{-1} for all targets.

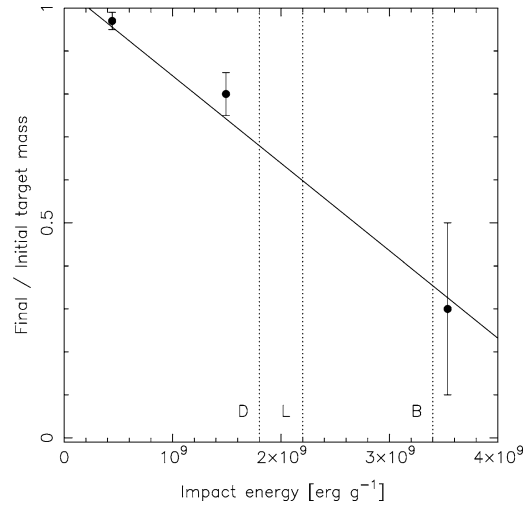

Fig. 5. Fraction of target mass that remains bounded after the impact in dependence of the specific impact energy Q. The dots are the averages over all our experiments and the error bars represent the maximum excursions. The estimates are computed 300 s after the impact. The dotted vertical lines are the catastrophic threshold estimated by: Davis et al. (1995) (D); Love and Ahrens (1996) (L); Benz and Asphaug (1999) (B). The solid line is the best fit $1.04–0.2 \times 10^{-9} Q$.

4.3. Spin distribution

Figure 6 shows the histogram of the post-impact intrinsic spins of the individual fragments. The results are analyzed 300 s after the impact of projectile P2 onto target N200. We recall that, for most fragments, the pre-impact spins (at $t = 0$) are close to zero. The most striking result are the relatively fast spin rates of most fragments, that range from periods of 2 h to a few of minutes. We may note that these spin rates are overestimated due to the value of κ used in the moment of inertia of the ellipsoids. Indeed, for a given parti-

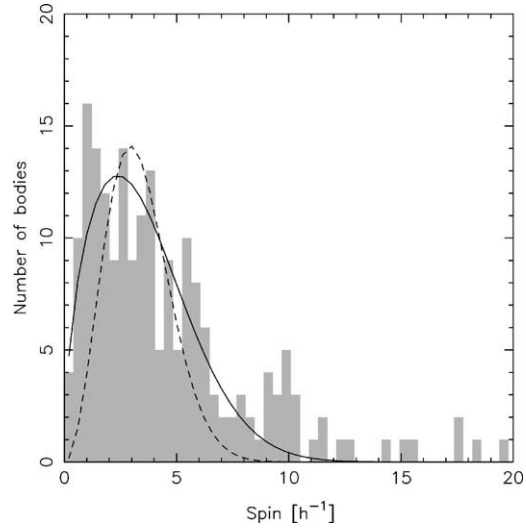

Fig. 6. Histogram of the intrinsic spins, 300 s after the impact of projectile P2 onto target N200. The impact occurs at an angle $\zeta = 0°$. The target is rotating with 4 h period. The solid curve is the best fit Eq. (44) with $n = 1/2$. The dashed curve corresponds to a Maxwellian fit.

tion of the rotational energy during the impact, the resulting spins should be roughly multiplied by a factor of $\sqrt{5/(2\kappa)}$ to account for the fact that the density distribution of the ellipsoids is not uniform. Since in all our examples $\kappa \simeq 10$, the above periods should be roughly multiplied by a factor of 2. In any case, most fragments have periods below the minimum of ~ 2–4 h allowed for strength-less bodies (Weidenschilling, 1981), and this is compatible with our assumption of monolithic fragments. We must recall that such fast rotation rates have only been detected in meter sized asteroids, while the smallest fragments in our experiments have a few kilometers. Notwithstanding, there is theoretical evidence that fast rotation would be possible in large porous bodies (Holsapple, 2001), and our results are also in agreement with simulations by Asphaug and Scheeres (1999) that provide very short rotational periods—ranging over two orders of magnitude—for kilometer sized fragments.

Another notable result from Fig. 6 is that the post-impact spin distribution cannot be fit with a Maxwellian. Indeed, there is a clear excess of slow and fast rotators with respect to the Maxwellian distribution. We try different fits by the function

$$f(x) = ax^n e^{-x^2/b^2} \tag{44}$$

assuming different values of n. The fits are done using a Levenberg–Marquardt algorithm (Press et al., 1997) to find a and b. The minimum residuals are obtained with $n = 0.5$ and this best fit is shown by the solid curve in Fig. 6. The dashed curve represents the Maxwellian fit with $n = 2$. The residuals in this case are more than twice or three times the residuals from the best fit.

We recall that it is usually assumed that a Maxwellian distribution would be the natural end state of any spin-relaxed population. For example, the distribution of asteroid rotation rates is approached to a Maxwellian (e.g., Harris and Burns, 1979; Farinella et al., 1981; Binzel et al., 1989; Fulchignoni et al., 1995). Our best fit with exponent $n = 0.5$ is in line with the above idea. It would be indicating that the spins are highly "thermalized" after the impact, and that any relaxation of the fragments' spins is achieved over time-scales much larger than our integration time span. We must bear in mind that the present state of the model does not allow to simulate the long term evolution of the spins because the multipole expansion of the gravitational potential is not accounted for (Scheeres et al., 2000). Moreover, if substantial re-accumulation takes place, the individual spin of the fragments is no longer relevant.

Figure 7 compares the best fits of the spin distributions for different impact energies. The fits are normalized such that

$$\int_0^\infty f(x)\,\mathrm{d}x = \frac{1}{2}ab^{n+1}\Gamma\big((n+1)/2\big) = 1, \tag{45}$$

where $\Gamma(n)$ is the gamma function. As expected, the distributions are wider for larger impact energies. However, the

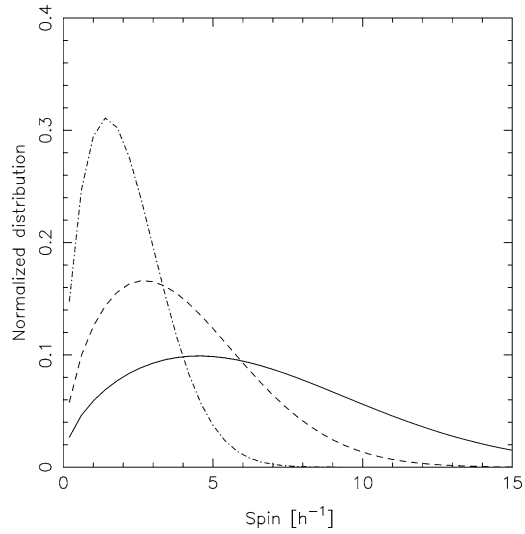

Fig. 7. Best fits of spin distributions, 300 s after the impact, for three different impact energies: with projectile P1 (dotted-dashed line), with projectile P2 (dashed line), and with projectile P3 (solid line). All examples correspond to target N200, rotating with 12 h period, and impacted at an angle $\zeta = 45°$. The distributions are normalized as explained in the text.

width of the distributions may change significantly over the integration time span. This happens in the examples with projectile P1, since most fragments re-accumulate very soon after the impact and the subsequent dissipation slows their spins. On the other hand, the spin distributions from the examples with projectiles P2 and P3 do not significantly change during the integrations.

The post-impact spins as a function of the fragments' size are shown in Fig. 8. In most cases, the fragments have rotational periods larger than the original period of the target. The data may be fit by a power law, although a large dispersion of spin values is observed among the smallest fragments. Typical values of the power law exponent are in the range -1.0 to -1.4. These values are smaller than the theoretical exponent -2.5 obtained by assuming equipartition of rotational kinetic energy. In fact, this latter power law rather gives the upper limit of the spin distribution at each fragment size. This situation is similar to the distribution of ejection velocities, and we may conclude that energy equipartition is never satisfied during a collision.

Since the acquired spin mostly depends on the moment of inertia of each fragment, the above results could actually change if we change the shape of the ellipsoids. For example, we may expect that considering more spherical fragments the spin distributions would be even narrower than those of Figs. 6–7, although the power law exponent would not change significantly. However, additional simulations are needed in order to confirm this idea.

4.4. Tumbling distribution

In order to characterize the tumbling state of each fragment after the impact, we follow Scheeres et al. (1998, 2000) and introduce the effective moment of inertia, I_i^{eff}, defined

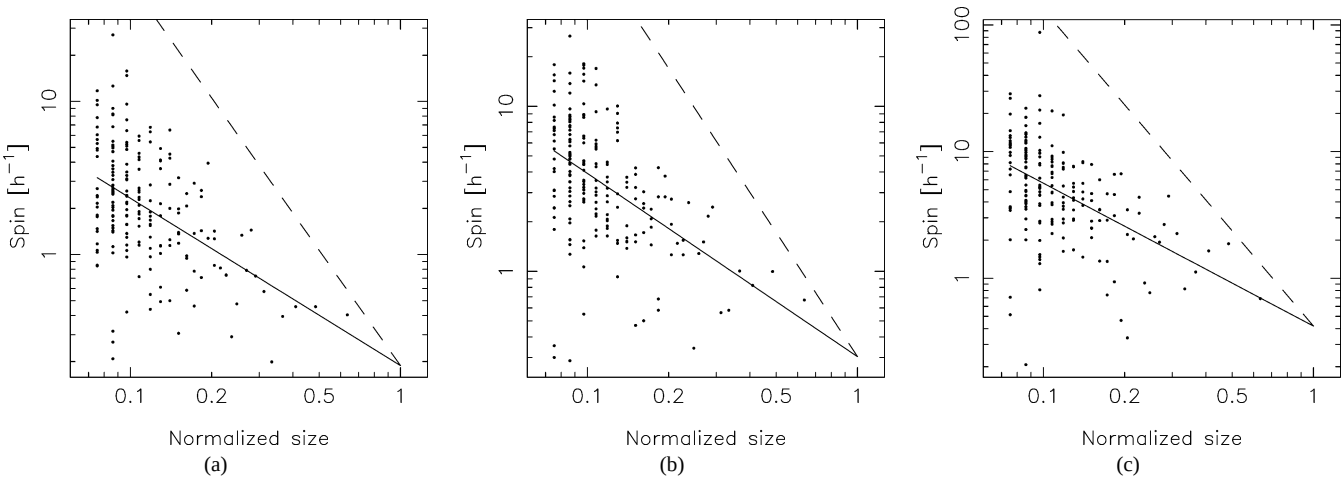

Fig. 8. Post-impact intrinsic spins vs. fragments' size (normalized to the size of the parent body), 300 s after the impact. The results correspond to target N200, rotating with period 4 h, and impacted at an angle $\zeta = 45°$ by projectile P1 (a), P2 (b), and P3 (c). The solid line is the power law best fit with exponent -1.09 (a), -1.11 (b), and -1.13 (c). The dashed line is the theoretical power law with exponent $-5/2$.

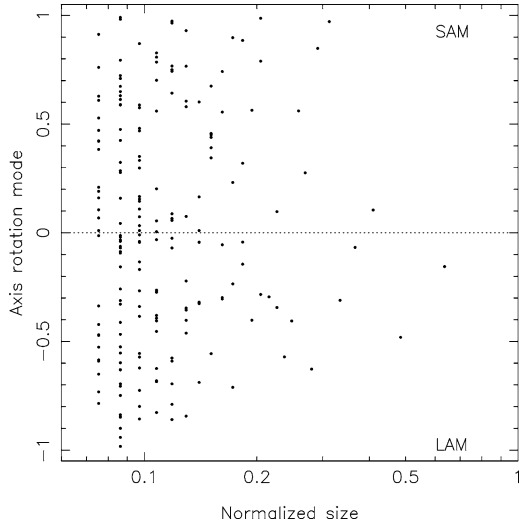

Fig. 9. Axis rotation mode vs. fragments size (normalized to the size of the parent body), 300 s after the impact. The results correspond to target N200, rotating with period 12 h, and impacted by projectile P2. The projectile impacted at an angle $\zeta = 90°$. Positive and negative values in the vertical axis correspond to rotation in short-axis mode (SAM) and long-axis mode (LAM), respectively.

as

$$I_i^{\rm eff} = \frac{|\mathbf{L}_{{\rm S},i}|^2}{2\mathcal{K}_{{\rm R},i}}, \tag{46}$$

where $\mathbf{L}_{{\rm S},i} = \mathbf{I}_i \boldsymbol{\omega}_i$ is the intrinsic angular momentum of spin and $\mathcal{K}_{{\rm R},i} = \boldsymbol{\omega}_i^{\rm T} \mathbf{I}_i \boldsymbol{\omega}_i / 2$ is the intrinsic rotational kinetic energy, both computed from Eqs. (4) and (23). This parameter is used to define the axis rotation mode of the fragment. Since $I_i^x \leqslant I_i^y \leqslant I_i^z$, the fragment is in a short-axis rotation mode (SAM) if $I_i^y < I_i^{\rm eff} \leqslant I_i^z$ or in a long-axis rotation mode (LAM) if $I_i^x \leqslant I_i^{\rm eff} < I_i^y$.

Figure 9 shows the axis rotation mode of the fragments a few minutes after the impact, in dependence of their size. The values of $I_i^{\rm eff} - I_i^y$ in the ordinates has been normalized such that 1 corresponds to a pure SAM, -1 corresponds to a pure LAM, and 0 corresponds to a pure middle-axis rotation mode. In all our examples, we find that most fragments after the impact are in a complex tumbling regime, like in this figure, and they keep this spinning state over the integration time span. In fact, we should not expect that the tumbling state of an ellipsoid changes, unless it re-accumulates with other ellipsoids or the model accounts for the gravitational multipole. Only in a few cases we detect some fragments in a nearly pure rotation around one axis. This is in good agreement with the simulations by Asphaug and Scheeres (1999) which found a full spectrum of rotational states ranging from nearly pure SAM to nearly pure LAM.

The above results are compatible with the idea that asteroids in a complex rotational state, like 4179 Toutatis, have been involved in recent collisional events, while the principal axis rotation observed in most asteroids is a consequence of their collisional and tidal evolution over very long time scales.

5. Conclusions

The above numerical examples show that our model describes fairly well the basic macroscopic features of the collisional dynamics of rubble-piles impacted by high-velocity projectiles. The model provides reasonable estimates for the energy partition and the ejection velocities. The rather fast spin rates of the resulting fragments and their tumbling states are in agreement with recent results based on hydrocodes. We may conclude that the behavior of the different observables predicted by our model is within expected ranges according to the typical impact energies considered.

Our model is based on a pure mechanical approach, expressed in terms of well-defined Lagrangian and dissipation functions, and has the advantage of being conceptually very simple. In spite of its simplicity, it has the minimal char-

acteristics to model the evolution of the attitude and spin of individual fragments. At this level, the model can provide an insight of the physical processes underneath the catastrophic collision of rubble-piles. Therefore, it may be applied to study some problems of Solar System dynamics, like the dynamical properties of fragments from recent collisional events (e.g., Nesvorný et al., 2002). Moreover, since the model is physically well-defined, it can be used as a kind of benchmark to test whether some ingredient is missing when the model does not reproduce the expected behavior of the problem under analysis.

In a forthcoming work we plan to extend the present study to analyze the long term re-accumulation processes after breakup events and the possible formation of contact binaries and satellites. The code may be modified in order to allow the projectile to be a rubble-pile too, and this could be applied to study low-velocity impacts, like those arising during planetesimal accretion (e.g., Leinhardt et al., 2000). Finally, we intend to incorporate to the model some additional effects, like the gravitational multipole interactions and the solar or planetary perturbations. We expect that this will allow us to model the tidal disruption of rubble-piles.

Acknowledgments

We thank C.E. Aguiar for fruitful discussions at the early stages of the model and for the crucial suggestion to use the quaternion variables. The comments and criticism of the two referees have helped to improve the manuscript and were highly appreciated. This work has been supported by CNPq, CAPES, and FAPERJ.

Appendix A. Dissipation function with additional conservation law

Consider the dynamics of the system of ellipsoids described by Eqs. (28) and (37). The effective Lagrangian is given by Eqs. (27) and (30), and the dissipation function is given by Eq. (41). Suppose that the system has a symmetry, so that the effective Lagrangian is invariant under the transformation: $\mathbf{r}_i \to \mathbf{r}_i + \delta\mathbf{r}_i$ and $\mathbf{q}_i \to \mathbf{q}_i + \delta\mathbf{q}_i$. In addition, suppose that this transformation may be expressed in terms of the variation of a given parameter, $\boldsymbol{\chi}$, as:

$$\delta\mathbf{r}_i = \delta\boldsymbol{\chi}\frac{\partial\mathbf{r}_i}{\partial\boldsymbol{\chi}}, \qquad \delta\mathbf{q}_i = \delta\boldsymbol{\chi}\frac{\partial\mathbf{q}_i}{\partial\boldsymbol{\chi}}. \tag{A.1}$$

The symmetry of the system is represented by the condition

$$\begin{aligned}\delta\widetilde{\mathcal{L}} &= \sum_{i=1}^{N}\left(\delta\mathbf{r}_i\frac{\partial\mathcal{L}}{\partial\mathbf{r}_i} + \delta\dot{\mathbf{r}}_i\frac{\partial\mathcal{L}}{\partial\dot{\mathbf{r}}_i} + \delta\mathbf{q}_i\frac{\partial\widetilde{\mathcal{L}}}{\partial\mathbf{q}_i} + \delta\dot{\mathbf{q}}_i\frac{\partial\mathcal{L}}{\partial\dot{\mathbf{q}}_i}\right)\\ &= \sum_{i=1}^{N}\delta\mathbf{r}_i\left(\dot{\mathbf{u}}_i - \frac{\partial\mathcal{F}}{\partial\dot{\mathbf{r}}_i}\right) + \sum_{i=1}^{N}\delta\dot{\mathbf{r}}_i\frac{\partial\mathcal{L}}{\partial\dot{\mathbf{r}}_i}\\ &\quad + \sum_{i=1}^{N}\delta\mathbf{q}_i\left(\dot{\mathbf{p}}_i - \frac{\partial\mathcal{F}}{\partial\dot{\mathbf{q}}_i}\right) + \sum_{i=1}^{N}\delta\dot{\mathbf{q}}_i\frac{\partial L}{\partial\dot{\mathbf{q}}_i}\\ &= \sum_{i=1}^{N}\frac{\mathrm{d}}{\mathrm{d}t}(\delta\mathbf{r}_i\,\mathbf{u}_i + \delta\mathbf{q}_i\,\mathbf{p}_i) - \sum_{i=1}^{N}\left(\delta\mathbf{r}_i\frac{\partial\mathcal{F}}{\partial\dot{\mathbf{r}}_i} + \delta\mathbf{q}_i\frac{\partial\mathcal{F}}{\partial\dot{\mathbf{q}}_i}\right)\\ &= 0,\end{aligned} \tag{A.2}$$

and this condition defines a conservation law of the system. If $\mathcal{F} \equiv 0$, the quantity

$$\mathbf{L} = \sum_{i=1}^{N}\left(\frac{\partial\mathbf{r}_i}{\partial\boldsymbol{\chi}}\mathbf{u}_i + \frac{\partial\mathbf{q}_i}{\partial\boldsymbol{\chi}}\mathbf{p}_i\right) \tag{A.3}$$

is a constant of motion. When the change in the coordinates is a pure translation, $\mathbf{L}$ is the total linear momentum of the system

$$\mathbf{L} = \sum_{i=1}^{N}\mathbf{u}_i. \tag{A.4}$$

In the case of a pure rotation we get the total angular momentum

$$\mathbf{L} = \sum_{i=1}^{N}(\mathbf{r}_i \times \mathbf{u}_i + \boldsymbol{\Omega}_i\mathbf{p}_i) \tag{A.5}$$

with

$$\boldsymbol{\Omega}_i = \frac{1}{2}\begin{pmatrix}\delta_i & -\gamma_i & \beta_i & -\alpha_i\\ \gamma_i & \delta_i & -\alpha_i & -\beta_i\\ -\beta_i & \alpha_i & \delta_i & -\gamma_i\end{pmatrix}. \tag{A.6}$$

Note, however, that even if $\mathcal{F} \neq 0$ it is possible to preserve $\mathbf{L}$ provided that

$$\sum_{i=1}^{N}\left(\frac{\partial\mathbf{r}_i}{\partial\boldsymbol{\chi}}\frac{\partial\mathcal{F}}{\partial\dot{\mathbf{r}}_i} + \frac{\partial\mathbf{q}_i}{\partial\boldsymbol{\chi}}\frac{\partial\mathcal{F}}{\partial\dot{\mathbf{q}}_i}\right) = 0. \tag{A.7}$$

We will now show that the point dissipation function Eq. (40) fulfills the above condition. For any pair i, j of ellipsoids we have

$$\mathcal{F}_{ij} = -\int_{-\infty}^{\infty}\mathrm{d}^3\mathbf{r}\,\rho_i(\mathbf{r})\rho_j(\mathbf{r})\mathbf{v}_{ij}^2, \tag{A.8}$$

where $\mathbf{v}_{ij} = \dot{\mathbf{r}}_i - \dot{\mathbf{r}}_j + \dot{\mathbf{R}}_i^{\mathrm{T}}\mathbf{s}^{(i)} - \dot{\mathbf{R}}_j^{\mathrm{T}}\mathbf{s}^{(j)}$, and Eq. (A.7) becomes

$$\begin{aligned}&\sum_{k=i,j}\left(\frac{\partial\mathbf{r}_k}{\partial\boldsymbol{\chi}}\frac{\partial\mathcal{F}_{ij}}{\partial\dot{\mathbf{r}}_k} + \frac{\partial\mathbf{q}_k}{\partial\boldsymbol{\chi}}\frac{\partial\mathcal{F}_{ij}}{\partial\dot{\mathbf{q}}_k}\right)\\ &\quad = -2\int_{-\infty}^{\infty}\mathrm{d}^3\mathbf{r}\,\rho_i(\mathbf{r})\rho_j(\mathbf{r})\\ &\qquad \times\left\{\sum_{k=i,j}\left(\frac{\partial\mathbf{r}_k}{\partial\boldsymbol{\chi}}\frac{\partial\mathbf{v}_{ij}^{\mathrm{T}}}{\partial\dot{\mathbf{r}}_k} + \frac{\partial\mathbf{q}_k}{\partial\boldsymbol{\chi}}\frac{\partial\mathbf{v}_{ij}^{\mathrm{T}}}{\partial\dot{\mathbf{q}}_k}\right)\right\}\mathbf{v}_{ij}.\end{aligned} \tag{A.9}$$

But it is straightforward to prove that

$$\frac{\partial \mathbf{v}_{ij}^{\mathrm{T}}}{\partial \dot{\mathbf{r}}_i} = \frac{\partial \mathbf{r}^{\mathrm{T}}}{\partial \mathbf{r}_i}, \qquad \frac{\partial \mathbf{v}_{ij}^{\mathrm{T}}}{\partial \dot{\mathbf{r}}_j} = -\frac{\partial \mathbf{r}^{\mathrm{T}}}{\partial \mathbf{r}_j},$$
$$\frac{\partial \mathbf{v}_{ij}^{\mathrm{T}}}{\partial \dot{\mathbf{q}}_i} = \frac{\partial \mathbf{r}^{\mathrm{T}}}{\partial \mathbf{q}_i}, \qquad \frac{\partial \mathbf{v}_{ij}^{\mathrm{T}}}{\partial \dot{\mathbf{q}}_j} = -\frac{\partial \mathbf{r}^{\mathrm{T}}}{\partial \mathbf{q}_j}, \tag{A.10}$$

where $\mathbf{r} = \mathbf{r}_i + \mathbf{R}_i^{\mathrm{T}}\mathbf{s}^{(i)} = \mathbf{r}_j + \mathbf{R}_j^{\mathrm{T}}\mathbf{s}^{(j)}$. Therefore

$$\sum_{k=i,j}\left(\frac{\partial \mathbf{r}_k}{\partial \boldsymbol{\chi}}\frac{\partial \mathbf{r}^{\mathrm{T}}}{\partial \mathbf{r}_k} + \frac{\partial \mathbf{q}_k}{\partial \boldsymbol{\chi}}\frac{\partial \mathbf{r}^{\mathrm{T}}}{\partial \mathbf{q}_k}\right) = \frac{\partial \mathbf{r}^{\mathrm{T}}}{\partial \boldsymbol{\chi}} - \frac{\partial \mathbf{r}^{\mathrm{T}}}{\partial \boldsymbol{\chi}} = 0 \tag{A.11}$$

and this condition is satisfied for all the pairs i, j of ellipsoids in the system. This proves that the point dissipation function preserves the total linear and angular momentum of the system.

References

Asphaug, E., Scheeres, D.J., 1999. Deconstructing Castalia. Evaluating a postimpact state. Icarus 139, 383–386.

Benz, W., Asphaug, E., 1994. Impact simulations with fracture I. Methods and tests. Icarus 107, 98–116.

Benz, W., Asphaug, E., 1999. Catastrophic disruptions revisited. Icarus 142, 5–20.

Benz, W., Asphaug, E., Ryan, E.V., 1994. Numerical simulations of catastrophic disruption: recent results. Planet. Space Sci. 42, 1053–1066.

Binzel, R.P., Farinella, P., Zappalà, V., Cellino, A., 1989. Asteroid rotation rates: distribution and statistics. In: Binzel, R.P., et al. (Eds.), Asteroids II. Univ. of Arizona Press, Tucson, pp. 416–441.

Bottke, W.F., Richardson, D.C., Michel, P., Love, S.G., 1999. 1620 Geographos and 433 Eros: shaped by planetary tides? Astron. J. 117, 1921–1928.

Cellino, A., Michel, P., Tanga, P., Zappalà, V., 1999. The velocity-size relationship for members of asteroid families and implications for the physics of catastrophic collisions. Icarus 141, 79–95.

Chapman, C.R., 7 colleagues, 1995. Discovery and physical properties of Dactyl, a satellite of Asteroid 243 Ida. Nature 374, 783.

Davis, D.R., Ryan, E.V., Farinella, P., 1995. On how to scale disruptive collisions. In: Proc. Lunar Planet. Sci. Conf. 26th, pp. 319–320. Abstract.

Dohnanyi, J., 1969. Collisional model of asteroids and their debris. J. Geophys. Res. 74, 2531–2554.

Durda, D.D., Greenberg, R., Jedicke, R., 1998. Collisional models and scaling laws: a new interpretation of the shape of the Main Belt asteroid size distribution. Icarus 135, 431–440.

Farinella, P., Paolicchi, P., Zappalà, V., 1981. Analysis of the spin rate distribution of asteroids. Astron. Astrophys. 104, 159–165.

Farinella, P., Davis, D.R., 1992. Collision rates and impact velocities in the Main Asteroid Belt. Icarus 97, 111–123.

Fujiwara, A., Tsukamoto, A., 1980. Experimental study on the velocity of fragments in collision breakup. Icarus 44, 142–153.

Fujiwara, A., Tsukamoto, A., 1981. Rotation of fragments in catastrophic impact. Icarus 48, 329–334.

Fulchignoni, M., Barucci, M.A., Di Martino, M., Dotto, E., 1995. On the evolution of asteroids spin. Astron. Astrophys. 299, 929–932.

Giblin, I., Martelli, G., Smith, P.N., Cellino, A., Di Martino, M., Zappalà, V., Farinella, P., Paolicchi, P., 1994. Field fragmentation of macroscopic targets simulating asteroidal catastrophic collisions. Icarus 110, 203–224.

Giblin, I., Martelli, G., Farinella, P., Paolicchi, P., Di Martino, M., Smith, P.N., 1998. The properties of fragments from catastrophic disruption events. Icarus 134, 77–112.

Gingold, R.A., Monaghan, J.J., 1977. Smothed particle hydrodynamics: theory and applications to non spherical stars. Mon. Not. R. Astron. Soc. 181, 375–389.

Harris, A.W., Burns, J.A., 1979. Asteroid rotation rates. I. Tabulation and analysis of rates, pole positions and shapes. Icarus 40, 115–144.

Holsapple, K.A., 1994. Catastrophic disruptions and cratering of Solar System bodies: a review and new results. Planet. Space Sci. 42, 1067–1078.

Holsapple, K.A., 2001. Equilibrium configurations of solid cohesionless bodies. Icarus 154, 432–448.

Housen, K.R., Holsapple, K.A., 1990. On the fragmentation of asteroids and planetary satellites. Icarus 84, 226–253.

Housen, K.R., Holsapple, K.A., 1999. Scale effects in strength-dominated collisions of rocky asteroids. Icarus 142, 21–33.

Kwiatkowski, T., 1995. Sideral period, pole and shape of Asteroid 1620 Geographos. Astron. Astrophys. 294, 274–277.

Leinhardt, Z.M., Richardson, D.C., Quinn, T., 2000. Direct N-body simulations of rubble pile collisions. Icarus 146, 133–151.

Leinhardt, Z.M., Richardson, D.C., 2002. N-body simulations of planetesimal evolution: effect of varying impactor mass ratio. Icarus 159, 306–313.

Love, S.G., Ahrens, T.J., 1996. Catastrophic impacts on gravity dominated asteroids. Icarus 124, 141.

Love, S.G., Hoerz, F., Brownlee, D.E., 1993. Target porosity effects in impact cratering and collisional disruption. Icarus 105, 216–224.

Lucy, L.B., 1977. A numerical approach to the testing of the fission hypothesis. Astron. J. 82, 1013–1024.

Melosh, H.J., Ryan, E.V., 1997. Asteroids: shattered but not dispersed. Icarus 129, 562–564.

Merline, W.J., 5 colleagues, 1999. Discovery of a moon orbiting the Asteroid 45 Eugenia. Nature 401, 565–568.

Michel, P., Benz, W., Tanga, P., Richardson, D.C., 2001. Collisions and gravitational re-accumulation: forming asteroid families and satellites. Science 294, 1696–1700.

Michel, P., Tanga, P., Benz, W., Richardson, D.C., 2002. Formation of asteroid families by catastrophic disruption: simulations with fragmentation and gravitational re-accumulation. Icarus 160, 10–23.

Miller, J.K., 6 colleagues, 2002. Determination of shape, gravity, and rotational state of Asteroid 433 Eros. Icarus 155, 3–17.

Nakamura, A., Fujiwara, A., 1991. Velocity distribution of fragment formed in a simulated collision disruption. Icarus 92, 132–146.

Nesvorný, D., Bottke, W.F., Dones, L., Levison, H.F., 2002. The recent breakup of an asteroid in the Main Belt region. Nature 417, 720–721.

Paolicchi, P., Burns, J.A., Weidenschilling, S.J., 2003. Side effects of collisions: spin rate changes, tumbling rotation states and binary asteroids. In: Bottke, W.F., et al. (Eds.), Asteroids III. Univ. of Arizona Press, Tucson, pp. 517–526.

Paolicchi, P., Cellino, A., Farinella, P., Zappalà, V., 1989. A semi-empirical model of catastrophic breakup processes. Icarus 77, 187–212.

Petit, J.-M., Farinella, P., 1993. Modelling the outcomes of high-velocity impacts between Solar System bodies. Celest. Mech. Dyn. Astr. 57, 1–28.

Pravec, P., Harris, A.W., 2000. Fast and slow rotation of asteroids. Icarus 148, 12–20.

Press, W.H., Teukolsky, S.A., Vetterling, W.T., Flannery, B.P., 1997. Numerical Recipes in Fortran 77. Cambridge Univ. Press, Cambridge.

Richardson, D.C., Quinn, T., Stadel, J., Lake, G., 2000. Direct large-scale N-body of planetesimal dynamics. Icarus 143, 45–59.

Richardson, D.C., Leinhardt, Z.M., Melosh, H.J., Bottke, W.F., Asphaug, E., 2003. Gravitational aggregates: evidence and evolution. In: Bottke, W.F., et al. (Eds.), Asteroids III. Univ. of Arizona Press, Tucson, pp. 501–515.

Ryan, E.V., 1992. Catastrophic collisions: laboratory impact experiments, hydrocode simulations, and the scaling problem. PhD thesis. Univ. of Arizona Press, Tucson.

Ryan, E.V., Melosh, H.J., 1998. Impact fragmentation: from the laboratory to asteroids. Icarus 133, 1–24.

Scheeres, D.J., Ostro, S.J., Hudson, R.S., DeJong, D.M., Suzuki, S., 1998. Dynamics of orbits close to Asteroid 4179 Toutatis. Icarus 132, 53–79.

Scheeres, D.J., Ostro, S.J., Werner, R.A., Asphaug, E., Hudson, R.S., 2000. Effects of gravitational interactions on asteroid spin states. Icarus 147, 106–118.

Thomas, P.C., 14 colleagues, 2002. Eros: shape, topography, and slope processes. Icarus 155, 18–37.

Veverka, J., 12 colleagues, 1997. NEAR's flyby of 253 Mathilde: images of a C asteroid. Science 278, 2109–2114.

Viateau, B., 2000. Mass and density of Asteroids 16 Psyche and 121 Hermione. Astron. Astrophys. 354, 725–731.

Yeomans, D.K., 8 colleagues, 1997. Estimating the mass of Asteroid 253 Mathilde from tracking data during the NEAR flyby. Science 278, 2109–2114.

Yeomans, D.K., 10 colleagues, 1999. Estimating the mass of Asteroid 433 Eros during the NEAR spacecraft flyby. Science 285, 560–561.

Weidenschilling, S.J., 1981. How fast can an asteroid spin? Icarus 46, 124–126.

Wetherill, G.W., 1967. Collisions in the asteroid belt. J. Geophys. Res. 72, 2429.

Whittaker, E.T., 1959. A Treatise on the Analytical Dynamics of Particles and Rigid Bodies. Cambridge Univ. Press, Cambridge.